Astronomy & Astrophysics

First multi-wavelength campaign on the gamma-ray-loud active galaxy IC 310

M. L. Ahnen[1], S. Ansoldi[2,25], L. A. Antonelli[3], C. Arcaro[4], A. Babić[5], B. Banerjee[6], P. Bangale[7],
U. Barres de Almeida[7,26], J. A. Barrio[8], J. Becerra González[9,10,27], W. Bednarek[11], E. Bernardini[12,28], A. Berti[2,29],
B. Biasuzzi[2], A. Biland[1], O. Blanch[13], S. Bonnefoy[8], G. Bonnoli[14], F. Borracci[7], T. Bretz[15,30], R. Carosi[14], A. Carosi[3],
A. Chatterjee[6], P. Colin[7], E. Colombo[9,10], J. L. Contreras[8], J. Cortina[13], S. Covino[3], P. Cumani[13], P. Da Vela[14],
F. Dazzi[7], A. De Angelis[4], B. De Lotto[2], E. de Oña Wilhelmi[16], F. Di Pierro[3], M. Doert[17], A. Domínguez[8],
D. Dominis Prester[5], D. Dorner[15], M. Doro[4], S. Einecke[17], D. Eisenacher Glawion[15,45,⋆], D. Elsaesser[17],
M. Engelkemeier[17], V. Fallah Ramazani[18], A. Fernández-Barral[13], D. Fidalgo[8], M. V. Fonseca[8], L. Font[19], C. Fruck[7],
D. Galindo[20], R. J. García López[9,10], M. Garczarczyk[12], M. Gaug[19], P. Giammaria[3], N. Godinović[5], D. Gora[12],
D. Guberman[13], D. Hadasch[21], A. Hahn[7], T. Hassan[13], M. Hayashida[21], J. Herrera[9,10], J. Hose[7], D. Hrupec[5],
G. Hughes[1], W. Idec[11], K. Ishio[7], K. Kodani[21], Y. Konno[21], H. Kubo[21], J. Kushida[21], D. Lelas[5], E. Lindfors[18],
S. Lombardi[3], F. Longo[2,29], M. López[8], P. Majumdar[6], M. Makariev[22], K. Mallot[12], G. Maneva[22], M. Manganaro[9,10],
K. Mannheim[15], L. Maraschi[3], M. Mariotti[4], M. Martínez[13], D. Mazin[7,21], U. Menzel[7], R. Mirzoyan[7], A. Moralejo[13],
E. Moretti[7], D. Nakajima[21], V. Neustroev[18], A. Niedzwiecki[11], M. Nievas Rosillo[8], K. Nilsson[18,31], K. Nishijima[21],
K. Noda[7], L. Nogués[13], M. Nöthe[17], S. Paiano[4], J. Palacio[13], M. Palatiello[2], D. Paneque[7], R. Paoletti[14],
J. M. Paredes[20], X. Paredes-Fortuny[20], G. Pedaletti[12], M. Peresano[2], L. Perri[3], M. Persic[2,32], J. Poutanen[18],
P. G. Prada Moroni[23], E. Prandini[4], I. Puljak[5], J. R. Garcia[7], I. Reichardt[4], W. Rhode[17], M. Ribó[20], J. Rico[13], T. Saito[21],
K. Satalecka[12], S. Schroeder[17], T. Schweizer[7], S. N. Shore[23], A. Sillanpää[18], J. Sitarek[11], I. Snidaric[5],
D. Sobczynska[11], A. Stamerra[3], M. Strzys[7], T. Surić[5], L. Takalo[18], F. Tavecchio[3], P. Temnikov[22], T. Terzić[5],
D. Tescaro[4], M. Teshima[7,21], D. F. Torres[24], N. Torres-Albà[20], T. Toyama[7], A. Treves[2], G. Vanzo[9,10],
M. Vazquez Acosta[9,10], I. Vovk[7], J. E. Ward[13], M. Will[9,10], M. H. Wu[16]
(The MAGIC Collaboration),
F. Krauß[33], R. Schulz[34,15,35], M. Kadler[15], J. Wilms[35], E. Ros[36,37,38], U. Bach[36], T. Beuchert[35,15], M. Langejahn[15,35],
C. Wendel[15], N. Gehrels[39], W. H. Baumgartner[39], C. B. Markwardt[39], C. Müller[40],
V. Grinberg[41], T. Hovatta[42,43], and J. Magill[44]

(Affiliations can be found after the references)

ABSTRACT

Context. The extragalactic very-high-energy gamma-ray sky is rich in blazars. These are jetted active galactic nuclei that are viewed at a small angle to the line-of-sight. Only a handful of objects viewed at a larger angle are so far known to emit above 100 GeV. Multi-wavelength studies of such objects up to the highest energies provide new insights into the particle and radiation processes of active galactic nuclei.

Aims. We aim to report the results from the first multi-wavelength campaign observing the TeV detected nucleus of the active galaxy IC 310, whose jet is observed at a moderate viewing angle of $10°−20°$.

Methods. The multi-instrument campaign was conducted between 2012 November and 2013 January, and involved observations with MAGIC, *Fermi*, INTEGRAL, *Swift*, OVRO, MOJAVE and EVN. These observations were complemented with archival data from the AllWISE and 2MASS catalogs. A one-zone synchrotron self-Compton model was applied to describe the broadband spectral energy distribution.

Results. IC 310 showed an extraordinary TeV flare at the beginning of the campaign, followed by a low, but still detectable TeV flux. Compared to previous measurements in this energy range, the spectral shape was found to be steeper during the low emission state. Simultaneous observations in the soft X-ray band showed an enhanced energy flux state and a harder-when-brighter spectral shape behavior. No strong correlated flux variability was found in other frequency regimes. The broadband spectral energy distribution obtained from these observations supports the hypothesis of a double-hump structure.

Conclusions. The harder-when-brighter trend in the X-ray and VHE emission, observed for the first time during this campaign, is consistent with the behavior expected from a synchrotron self-Compton scenario. The contemporaneous broadband spectral energy distribution is well described with a one-zone synchrotron self-Compton model using parameters that are comparable to those found for other gamma-ray-emitting misaligned blazars.

Key words. galaxies: active – galaxies: individual: IC 310 – gamma rays: galaxies

---

⋆ Corresponding author: D. Eisenacher Glawion, e-mail: dglawion@lsw.uni-heidelberg.de

1. Introduction

An active galactic nucleus (AGN) emits radiation over a broad band of the electromagnetic spectrum. Radio-loud AGNs form a subclass in which plasma jets are found to be perpendicularly extending away from the central region consisting of an accretion disk and a supermassive black hole (BH). In the very-high-energy (VHE) gamma-ray range (50 GeV $\lesssim E \lesssim$ 50 TeV), sixty-six of these objects have been detected so far[1]. Most of these objects fall into the subcategory of blazars. They are characterized by strong variability in all energy bands and on all timescales. According to the unified scheme for radio-loud AGNs (Urry & Padovani 1995), blazars are believed to be AGNs viewed at a small angle between the jet-axis and the line-of-sight. Hence, a strong Doppler beaming effect is expected to play a major role in the explanation of the observational properties. Only a few of the detected VHE objects belong to the class of radio galaxies or misaligned blazars: Centaurus A (Aharonian et al. 2009), M 87 (Aharonian et al. 2003; 2006, Acciari et al. 2008, 2009; Albert et al. 2008), NGC 1275 (Aleksić et al. 2012, 2014b), IC 310 (Aleksić et al. 2010, 2014a,c), and PKS 0625−354 (Dyrda et al. 2015). Radio galaxies and misaligned blazars are viewed at a larger angle to the jet-axis; therefore, the Doppler boosting effect is smaller compared to blazars.

Due to the small Doppler-boosting effect and often measurable viewing angle, various acceleration and radiation models for the high-energy emission of radio-loud AGNs can be well studied for radio galaxies. This investigation requires multi-wavelength (MWL) data of such objects, preferably simultaneous and with good observational coverage due to their variable behavior. For all these objects, except for IC 310 and PKS 0625−354, extensive MWL campaigns up to the VHE range have been conducted and reported previously (Abdo et al. 2009b, 2010a; Acciari et al. 2009; Aleksić et al. 2014b).

IC 310 is located on the outskirts of the Perseus galaxy cluster with a redshift of z = 0.0189 (Bernardi et al. 2002). Originally, this object was classified as a head-tail radio galaxy (Ryle & Windram 1968; Miley 1980; Sijbring & de Bruyn 1998). However, observations in different frequency bands indicated that it is, in fact, a transitional object (Aleksić et al. 2014a) with a viewing angle of $10° \lesssim \theta \lesssim 20°$ (Aleksić et al. 2014c), showing properties similar to a radio galaxy, for example, extended radio emission on kpc scales, and a blazar, for example, a one-sided parsec-scale jet (Kadler et al. 2012). While weak optical emission lines observed from IC 310 are typically found in radio galaxies (Owen et al. 1996), Rector et al. (1999) identified IC 310 as possible low-luminosity BL Lac object. The X-ray emission is mostly point-like as observed with ROSAT and *XMM-Newton* (Schwarz et al. 1992; Rhee et al. 1994; Sato et al. 2005) whereas a hint of X-ray halo emission in the direction of the observed kpc radio jet has been reported by Dunn et al. (2010). In the soft X-ray band, the flux and spectrum vary in a manner typical for blazars (Aleksić et al. 2014a). In the gamma-ray band, IC 310 was first detected with the *Fermi*-Large Area Telescope (LAT) at energies above 30 GeV by Neronov et al. (2010) and with the MAGIC telescopes above 260 GeV (Aleksić et al. 2010).

In this paper we present the results from the first MWL campaign, conducted between 2012 and 2013. The publication is structured as follows: the observations of all participating instruments and the data analysis are described in Sect. 2 from higher to lower frequencies. In Sect. 3, the observational results

are presented. The assembled MWL light curve and spectral energy distribution (SED) will be discussed in Sect. 4, followed by the summary and conclusions in Sect. 5.

2. Multi-wavelength observations and data analysis

The MWL campaign for IC 310 in 2012 and 2013 included observations from radio up to the highest energies with space- and ground-based telescopes. Even while the campaign did not aim to observe the source in a high state, serendipitously a bright TeV flare with minute timescale variability was detected in 2012 November by MAGIC (Aleksić et al. 2014c). Participating instruments in the radio band were OVRO (single-dish) as well as the very-long-baseline interferometry (VLBI) arrays: European VLBI Network (EVN) and the VLBA through the "Monitoring Of Jets in Active galactic nuclei with VLBA Experiment" (MO-JAVE) project at cm wavelengths. In the optical and ultraviolet band, measurements were provided by KVA and *Swift*-UVOT. The X-ray regime was covered by *Swift*-XRT and -BAT, and IN-TEGRAL. *Fermi*-LAT and MAGIC permitted the high-energy (HE, 20 MeV $\lesssim E \lesssim$ 100 GeV) and VHE gamma-ray measurements. In the following section, the observations of IC 310 and the data analysis is described.

2.1. Very high energy: the MAGIC telescopes

MAGIC is a system of two Imaging Air Cherenkov telescopes, both 17 m in diameter, located on the Canary Island of La Palma, Spain. It covers the electromagnetic spectrum in the VHE range from 50 GeV to 50 TeV and achieves an angular resolution of ~0.1° (Aleksić et al. 2016b).

The observations during the MWL campaign were conducted after the upgrade of the two telescopes in 2011–2012 was completed (Aleksić et al. 2016a). On the first night of observation, 2012 November 12–13 (MJD 56 243.95–56 244.11), during 3.7 h of observation, MAGIC detected a bright flare as reported in Aleksić et al. (2014c). Further observations up to 2013 January 17 (MJD 56 309.1) were carried out as part of the MWL campaign during dark and moon time. Data affected by non-optimal weather conditions were discarded. Only observations during dark night and with moderate moon light were selected, and the standard analysis (Aleksić et al. 2016b) can be applied. After the selection, the data set consists of ~39 h including the data of the flaring night. The data cover the zenith distance range of 11° < Zd < 56°.

Data analysis was performed analogously to Aleksić et al. (2014c, 2016b). Image cleaning was performed using the dynamical sum-cleaning algorithm presented in Sitarek et al. (2013). The significance of the signal was calculated from Eq. (17) of Li & Ma (1983) using four background regions that do not overlap with the emission from NGC 1275, which is a VHE object 0.6° away from IC 310. Flux and differential upper limits are calculated according to Rolke et al. (2005) using a 95% confidence level. Following Aleksić et al. (2016b), we considered the following systematic errors for the spectra: 11% for the flux normalization, 15% for the energy scale and 0.15 for the photon index. As reported previously in Aleksić et al. (2014a,c), the absorption due to the extragalactic background light (EBL) is only marginal for IC 310. The intrinsic spectra presented in this paper are calculated using the model of Domínguez et al. (2011).

---

[1] http://tevcat.uchicago.edu/

2.2. High energy: Fermi-LAT

Fermi was launched in 2008 June and since 2008 August 5, it is operated primarily in sky survey mode, scanning the entire sky every three hours (Atwood et al. 2009). The *Fermi*-LAT is a pair-conversion telescope sensitive to photons between 20 MeV and several hundred GeV (Ackermann et al. 2012).

We calculated spectra using the *Fermi* Science Tools (v10r0p5)[2] for the time period 2012 November 01 (MJD 56 232) to 2013 January 31 (MJD 56 323). We used the Pass 8 data, the recommended *P8R2_SOURCE_V6* instrumental response functions, the isotropic diffuse background template *iso_P8R2_SOURCE_V6_v06* and the Galactic emission model *gll_iem_v06* (Acero et al. 2016)[3], a region of interest (ROI) with a radius of 10° and an energy range of 1–300 GeV. We ran the unbinned likelihood analysis with a 90° zenith angle cut to reduce contamination from the Earth limb. As an input for the likelihood analysis we used the 3FGL model (Acero et al. 2015). For sources within the ROI the photon index and prefactor (and equivalent for other models) were left free. Spectral upper limits are calculated with a limiting test statistic (TS) of 25 (Mattox et al. 1996), and taking into account sources in the spectral model of a radius of 20°. The predicted number of counts is low (approximately ten). Because NGC 1275 appears to be very bright and close to IC 310 with an offset of 0.6°, the results reported here are calculated for energies higher than 1 GeV to mitigate the effects of a larger point-spread function at lower energies[4].

2.3. X-ray: INTEGRAL, Swift-BAT/XRT

The International Gamma-Ray Astrophysics Laboratory (INTEGRAL) satellite has been in operation since late 2002 (Winkler et al. 2003). It is equipped with several instruments in the hard X-ray to soft gamma-ray range: the high resolution spectrometer SPI at 20 keV–8 MeV (Vedrenne et al. 2003), and two high angular resolution gamma-ray imagers, called IBIS, which operate at 15–1000 keV and 0.175–10.0 MeV (Ubertini et al. 2003).

The IBIS data were extracted using the Offline Science Analysis tool OSA, version 10.1. All data between 2012 August and 2013 February are taken into account, where IC 310 was located within 14° from the pointing center, resulting in 451 science windows. These data were filtered for the energy range between 20 keV and 200 keV. No significant signal was detected from these data and upper limits are derived. SPI data were not used for this publication.

The *Swift* satellite was launched in late 2004 (Ggehrels et al. 2004). *Swift* provides measurements with telescopes covering the optical and X-ray (soft and hard) ranges. Continuous observations in the hard X-ray range (15–150 keV), mainly for detecting gamma-ray bursts, are provided by the Burst Alert Telescope (BAT). The X-Ray Telescope (XRT) operates in the soft X-ray regime from 0.2 to 10 keV (Burrows et al. 2005).

We extracted a spectrum in the energy band of 20–100 keV from the 104-month *Swift*-BAT survey maps and fit the spectrum with a simple power law with fixed normalization.

A fitting-statistic for Poisson-distributed source count rates and Gaussian-distributed background count rates as recommended in the XSPEC statistics appendix was used[5]. The calculations of the flux, photon index, and the corresponding 90% uncertainties were implemented using Monte Carlo simulations of the spectrum.

Furthermore, observations of IC 310 with the *Swift*-XRT with a total exposure of 45.8 ks were performed in 2012 November and December. The results presented here are compared to earlier observations of 13.2 ks taken in January of the same year. The XRT data were reduced with standard methods, using the most recent software packages (HEASOFT 6.15.1 3) and calibration databases. Spectra were grouped to a minimum signal-to-noise ratio of five to ensure the validity of χ^2 statistics. For the broadband SED we applied another re-binning in order to increase the significance of individual points. Spectral fitting was performed with ISIS 1.6.2 (Houck & Denicola 2000). We fit the 0.5–10 keV energy band with an absorbed power-law model, which yielded a good fit probability. X-ray data were de-absorbed using abundances from Wilms et al. (2000) and cross sections from Verner et al. (1996). As previous *Chandra* observations (Aleksić et al. 2014a) revealed a N_H significantly above the Galactic N_H value of 0.12×10^{22} cm^{-2} for IC 310 (Kalberla et al. 2010) we left N_H free in the fit.

2.4. Ultraviolet and optical: Swift-UVOT, KVA

In addition to the X-ray instruments, *Swift* is equipped with the UltraViolet/Optical Telescope (UVOT) providing observations in the ultraviolet (UV) and optical ranges simultaneously with the XRT (Gehrels et al. 2004). The telescope is equipped with the following filters: V (547 nm), B (439 nm), U (347 nm), *UVW1* (260 nm), *UVM2* (225 nm), and *UVW2* (193 nm). Swift-UVOT data were extracted following standard methods[6].

The Kungliga Vetenskaps Akademien (KVA) telescopes are located at the Observatorio del Roque de los Muchachos on the island of La Palma, Spain, and are operated by the Tuorla observatory[7]. They consist of two optical telescopes with mirror diameters of 60 cm and 35 cm. Filters in the *R*-band (640 nm), *B*-band (550 nm), and *V*-band (440 nm) are available. The photometric observations were conducted with the *R*-band filter and the 35 cm telescope during the MAGIC observations. The data were analyzed using a standard semi-automatic pipeline. The brightness of the source was measured using differential photometry with a standard aperture radius of 5.0″. The host galaxy emission is expected to be constant. Any AGN variability would affect the light curve. Optical, infrared, and ultraviolet data were de-reddened using the same absorbing columns obtained from the *Swift*-XRT data (Nowak et al. 2012, and references therein).

2.5. Radio: OVRO, EVN, VLBA/MOJAVE

The 40 m Owens Valley Radio Observatory (OVRO, California, USA) telescope provides radio data for a list of AGNs at 15 GHz nearly twice per week since 2008[8]. Details on the observing strategy and the calibration procedures are summarized in Richards et al. (2011). The data presented in this paper cover

---

[2] Available online at http://fermi.gsfc.nasa.gov/ssc/data/analysis/software/

[3] http://fermi.gsfc.nasa.gov/ssc/data/access/lat/BackgroundModels.html

[4] The plot of the point-spread function can be found online at https://www.slac.stanford.edu/exp/glast/groups/canda/lat_Performance.htm

[5] https://heasarc.gsfc.nasa.gov/xanadu/xspec/manual/XSappendixStatistics.html

[6] http://swift.gsfc.nasa.gov/analysis/UVOT_swguide_v2_2.pdf

[7] http://users.utu.fi/kani/1m

[8] http://www.astro.caltech.edu/ovroblazars/

the time range from 2012 October 31 (MJD 56 231) to 2012 December 22 (MJD 56 283).

The European VLBI Network is a consortium of several radio-astronomical institutes and telescopes from Europe, Asia, and South Africa[9]. Due to the large collection area of its telescopes, the EVN provides excellent sensitivity to weak emission. For IC 310, observations in October and November 2012 at the frequencies 1.7, 5.0, 8.4, and 22.2 GHz were carried out.

The MOJAVE project is a long-term VLBI monitoring program at 15 GHz conducted with the Very Long Baseline Array (VLBA) as a continuation of the VLBA 2 cm survey, for example, Lister et al. (2016)[10]. The array consists of ten identical 25 m (in diameter) antennas with a baseline up to 8000 km. IC 310 was included in the target list of MOJAVE in early 2012.

A description of the analysis of the EVN data can be partially found in Aleksić et al. (2014c). More information on the data analysis procedure of the MOJAVE and OVRO data and an extended analysis of these data will be published in a separate paper (Schulz et al., in prep.), which will include additional observations made over a longer period of time that will allow the investigation of possible changes of the jet structure. Only the results of the OVRO observations during the campaign and EVN and MOJAVE flux density measurements are presented here as they are relevant to the study of the multi-band light curve and the SED.

2.6. Additional data

We also consider historical data of IC 310 for the SED from the Wide-Field Infrared Survey Explorer (WISE) and the Two Micron All Sky Survey (2MASS). The AllWISE Source Catalog (Wright et al. 2010) covers a time range from 2010 January to 2010 November, while the 2MASS catalog (Skrutskie et al. 2006) covers from 1997 June to 2001 February. The data were de-reddened using the absorption column derived from spectral fits to the X-ray observations.

3. Results

In this section we present the results from the MWL observation starting with the highest energies.

3.1. MAGIC results

During the period 2012 November to 2013 January (MJD 56 245.0–56 309.1), IC 310 was detected by MAGIC using data (excluding the flare data of MJD 56 244.0) over an effective time (observation time minus dead time) t_{eff} = 35.3 h with a significance of 5.22σ above 300 GeV. This low significance measured over a rather long time span indicates a low flux state after the flare. Here we have excluded the flare data from the data selection for two reasons. Firstly, to test the detection of the object outside of the flaring state and secondly, because a large part of the observations used for the MWL SED, for example, in X-rays, was performed at a time not simultaneouly with the TeV flare.

The energy spectrum (dN/dE) between 82 GeV and 2.1 TeV during the campaign from 2012 November to 2013 January (Fig. 1), excluding the flare data, can be described with the

---

[9] http://www.evlbi.org/
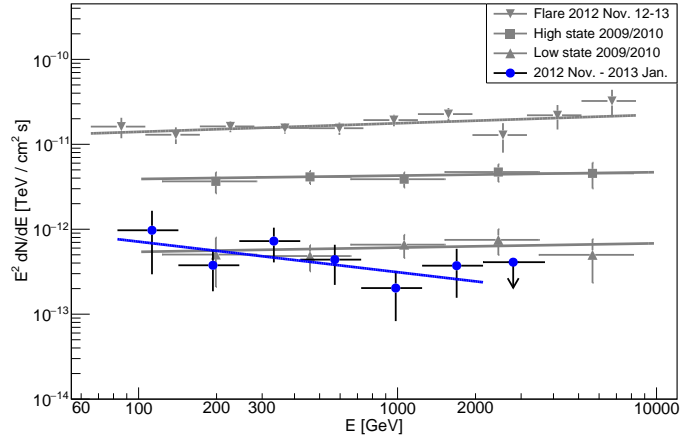[10] https://science.nrao.edu/facilities/vlba

Fig. 1. Measured spectra in the VHE band during different flux states obtained with MAGIC. The blue data points as well as the blue line show the resulting spectra from observations during 2012 November and 2013 January (excluding the large VHE flare from 2012 Nov. 12–13). Spectral results from previous publications (Aleksić et al. 2014a,c) are shown in gray for comparison.

Table 1. Division of the data of the flare in the night of 2012-11-12 to 2012-11-13 according to different flux states.

Period	Start time hh:mm:ss	Stop time hh:mm:ss	MJD start	MJD stop
Ia	22:50:49	23:10:35	56 243.951958	56 243.965686
Ib	23:55:20	01:16:14	56 243.996756	56 244.052941
II	23:11:21	23:51:18	56 243.966217	56 243.993958
III	01:16:52	01:36:36	56 244.053380	56 244.067083
IV	01:37:20	01:56:58	56 244.067593	56 244.081231
V	01:57:36	02:33:05	56 244.081669	56 244.106308

power-law function:

$$\frac{dN}{dE} = f_0 \times \left(\frac{E}{1\,\text{TeV}}\right)^{-\Gamma} \left[\frac{10^{-12}}{\text{cm}^2\,\text{s}\,\text{TeV}}\right], \quad (1)$$

with a flux normalization f_0 = $(3.12 \pm 0.91_{stat} \pm 0.34_{syst}) \times 10^{-13}\,\text{TeV}^{-1}\,\text{cm}^{-2}\,\text{s}^{-1}$ at 1 TeV and a photon spectral index of $\Gamma = (2.36 \pm 0.30_{stat} \pm 0.15_{syst})$. The normalization energy of 1 TeV was fixed and selected for easier comparison with previous measurements. As simultaneous *Swift*-XRT and UVOT data are only available for the 2012 November and December observations, we also calculated a MAGIC spectrum for the time period 2012 November to December in the same energy range. The resulting spectrum agrees, within the errors, with the spectrum calculated for the entire campaign. Thus, in the subsequent sections we only show and discuss the spectrum for the entire campaign.

We further investigated the change in the spectrum at different flux states by comparing our results with previous measurements, as well as by studying spectra of different flux states during the flare on 2012 November 12–13. In Aleksić et al. (2014a,c), no significant spectral variability was reported. Here, we present individual spectra during the flare. The division of the data of the flare according to different flux states is given in Table 1 and shown in Fig. 2. Besides the separations based on the fluxes, the definitions of the intervals are also determined by the duration of observing runs of typically 20 min. The resulting spectra are shown in Fig. 3 and their parameters are listed in Table 2.

In Fig. 4, we present for all temporally non-overlapping data the photon spectral index versus the integrated flux (overlapping
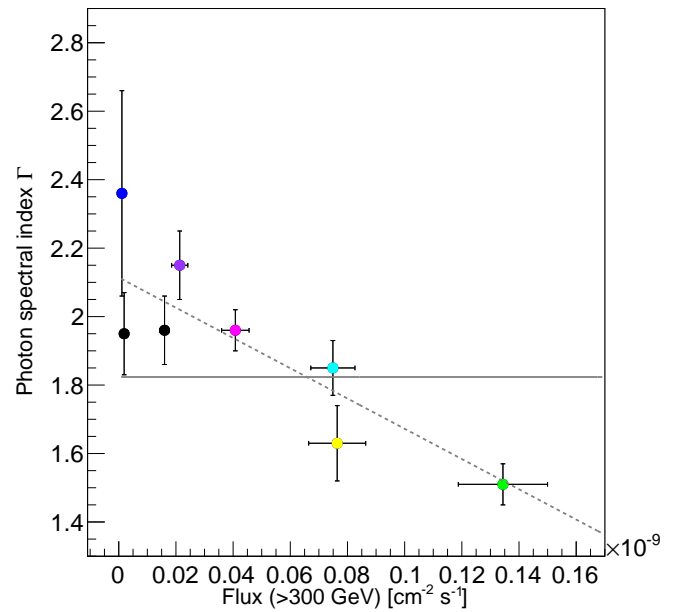
Table 2. Results of power-law spectra measured with MAGIC during different periods.

State	Comment	Energy range [TeV]	$f_0 \pm f_{stat} \pm f_{syst}$ $\times 10^{-12}$ [TeV^{-1} cm^{-2} s^{-1}]	$\Gamma \pm \Gamma_{stat} \pm \Gamma_{syst}$	References
high state 2009/2010	observed	0.12–8.1	4.28 ± 0.21 ± 0.73	1.96 ± 0.10 ± 0.20	Aleksić et al. (2014a)
low state 2009/2010	observed	0.12–8.1	0.608 ± 0.037 ± 0.11	1.95 ± 0.12 ± 0.20	Aleksić et al. (2014a)
flare Nov. 2012	observed	0.07–8.3	17.7 ± 0.9 ± 2.1	1.90 ± 0.04 ± 0.15	Aleksić et al. (2014c)
flare period Nov. 2012 I	observed	0.07–4.0	6.4 ± 0.8 ± 0.7	2.15 ± 0.10 ± 0.15	this work
flare period Nov. 2012 II	observed	0.07–9.5	13.5 ± 0.9 ± 1.5	1.96 ± 0.06 ± 0.15	this work
flare period Nov. 2012 III	observed	0.07–4.0	37.5 ± 4.2 ± 4.1	1.63 ± 0.11 ± 0.15	this work
flare period Nov. 2012 IV	observed	0.07–9.5	44.2 ± 2.1 ± 4.9	1.51 ± 0.06 ± 0.15	this work
flare period Nov. 2012 V	observed	0.07–9.5	27.5 ± 2.3 ± 3.0	1.85 ± 0.08 ± 0.15	this work
Nov. 2012–Jan. 2013	observed	0.08–2.1	0.31 ± 0.09 ± 0.03	2.36 ± 0.30 ± 0.15	this work
Nov. 2012–Jan. 2013	intrinsic	0.08–2.1	0.37 ± 0.11 ± 0.04	2.26 ± 0.30 ± 0.15	this work
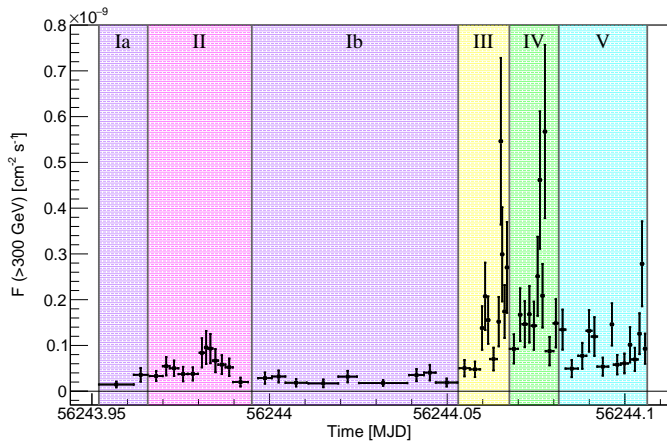
Fig. 2. Division of the MAGIC data taken during the night of 2012 November 12–13 into data sub-sets according to different flux states. The light curve data points are taken from Aleksić et al. (2014c). Vertical lines and colored boxes indicate the boundaries for the different flux periods used for the investigation of the spectral variability. The time intervals related to the above-mentioned periods are reported in Table 1.
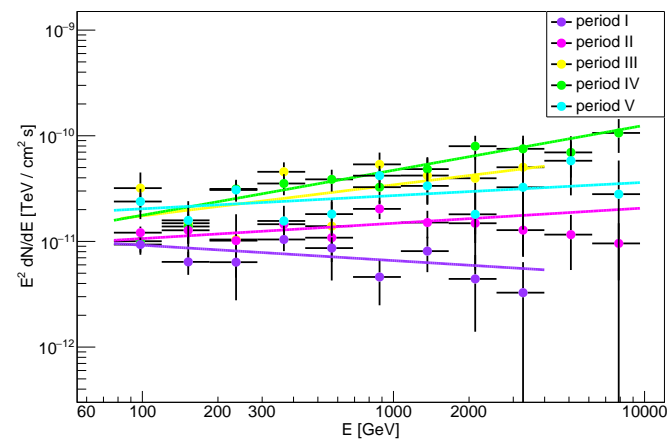
Fig. 3. Measured spectral energy distributions from different time periods during the night of the flare 2012 November 12–13 obtained by MAGIC. The time periods are given in Table 1 and indicated with lines in Fig. 2. The same color scheme as in Fig. 2 is used.

Fig. 4. Power-law index of VHE spectra as a function of the VHE flux above 300 GeV measured by MAGIC. The photon index values, which are not corrected for EBL absorption, are listed in Table 2. The color scheme is the same as the one used in Fig. 2 and in Fig. 3. In addition, the result for the multi-wavelength campaign is shown in blue, and the historical measurements from Aleksić et al. (2014a) are shown in black. The solid and dashed lines represent a constant and a linear fit, respectively.

previous measurements (Aleksić et al. 2014a) and from the data presented here. A constant fit to the data points in Fig. 4 reveals a χ^2/d.o.f. of 52.5/7, thus a low probability for being constant of 4.6×10^{-9}. A higher probability can be obtained with a linear function which yields a χ^2/d.o.f. of 7.0/6 and a probability of 0.32.

The mean integrated flux over the entire period was measured to be $F_{mean} = (1.59 \pm 0.29) \times 10^{-12}$ cm^{-2} s^{-1} above 300 GeV when excluding the data from the 2012 November flare. This is ~40 times lower than the mean integrated flux of $(6.08 \pm 0.29) \times 10^{-11}$ cm^{-2} s^{-1} reported for the 2012 November flare in Aleksić et al. (2014c). Due to the faint emission, a monthly light curve is computed. The light curve is calculated assuming a simple power-law distribution with a photon index of $\Gamma = 2.4$. For the data during the flare, a different photon index, $\Gamma = 2.0$, was used. The monthly calculated light curve is

data would include a bias so the averaged flare spectrum on 2012 November 12–13 is not included). All integrated fluxes represent mean fluxes and have been obtained by fitting all light curves above 300 GeV with a constant line, both the light curves from

Table 3. MAGIC gamma-ray flux measurements from single observations, as well as integrated over months.

Data used	MJD start	t_{eff} [h]	$F_{E>300\,\text{GeV}}$ [$10^{-12}\,\text{cm}^{-2}\,\text{s}^{-1}$]
all data (flare excl.)	...	35.3	1.59 ± 0.29
2012 Nov. (flare excl.)	...	17.9	1.69 ± 0.42
2012 Dec.	...	7.1	1.88 ± 0.61
2013 Jan.	...	10.4	$(0.61 \pm 0.54) < 2.09$
2012-11-13	56 243.95	3.51	61.82 ± 2.92
2012-11-14	56 245.00	2.37	<3.03
2012-11-16	56 246.94	3.47	<1.74
2012-11-18	56 249.11	2.39	<6.72
2012-11-19	56 249.99	4.41	<4.70
2012-11-21	56 252.06	1.30	<4.52
2012-11-22	56 253.09	1.96	<4.81
2012-11-23	56 254.13	1.30	6.43 ± 1.87
2012-11-24	56 255.17	0.65	<10.26
2012-12-15	56 275.93	0.92	<8.05
2012-12-16	56 276.82	0.65	<2.83
2012-12-17	56 277.83	2.01	<5.29
2012-12-18	56 278.83	3.50	3.26 ± 0.96
2013-01-10	56 301.89	0.62	5.71 ± 2.37
2013-01-11	56 302.88	0.65	<3.12
2013-01-13	56 304.87	0.80	<9.21
2013-01-14	56 305.82	0.98	<6.21
2013-01-15	56 306.83	1.50	<3.95
2013-01-16	56 307.83	2.50	2.22 ± 1.07
2013-01-17	56 308.82	3.34	<1.35

Notes. The dates given in the first column correspond to the day following the observation night. The upper limits were computed with a 95% confidence level.

shown in Fig. 9. Fitting this light curve with a constant reveals a flux of $F_{\text{const.}} = (1.42 \pm 0.29) \times 10^{-12}\,\text{cm}^{-2}\,\text{s}^{-1}$ with a χ^2/d.o.f. of 3.2/2 (probability of 0.20). Thus, no significant variability of the flux is found from month to month. Results from individual days are given in Table 3.

3.2. Fermi-LAT results

In the time range from 2012 November 01 (MJD 56 232) to 2013 January 31 (MJD 56 323), IC 310 could not be detected with *Fermi*-LAT (TS < 25) over the entire three months period. The measured light curve is shown in Fig. 9. Only upper limits of the flux and one flux point in 2013 January could be calculated. Thus, no further conclusion can be drawn on the variability behavior of IC 310. We also searched for individual gamma-ray event candidates in the *Fermi*-LAT detector during the MWL campaign. Within a circle with a radius of 10.0° around IC 310, only four events could be found above 1 GeV with a larger likelihood to originate from IC 310 than from NGC 1275 and a probability of higher than 50%. The probability for each photon was calculated using `gtsrcprob`. They were detected on MJD 56 248.4, 56 298.8, 56 303.7, and 56 318.1, with energies of 4.8, 8.0, 2.4, and 17.2 GeV, respectively. The arrival times are indicated with blue lines in Fig. 9. The calculated 95% confidence level upper limits for the SED are shown in Fig. 10. The blue upper limit spectrum covers the full time range of the campaign from 2012 November 01 to 2013 January 31 and an energy range from 1 GeV to 72 GeV.

3.3. X-ray

The light curve measured with *Swift*-XRT is shown in Fig. 5 and in Fig. 9. An overview of the results – for example, the flux level in the energy range of 2–10 keV, the photon index, and N_{H} – can be found in Table 4.

The temporal evolution of the flux in the energy range 2–10 keV, the photon index, and the column density N_{H} in 2012 November to December during the campaign is presented in Fig. 5. The mean energy flux has been measured to be $(0.61 \pm 0.01) \times 10^{-11}\,\text{erg}\,\text{cm}^{-2}\,\text{s}^{-1}$, which is about five times higher than during previous measurements (Aleksić et al. 2014a) and moderately higher (factor of 1.4) than in 2012 January (see Table 4). A fit to the light curve with a constant line reveals a probability of 7.3×10^{-7} for a constant energy flux of $(0.58 \pm 0.01) \times 10^{-11}\,\text{erg}\,\text{cm}^{-2}\,\text{s}^{-1}$ (χ^2/d.o.f. = 49.6/11). The observation on MJD 56 280.82 deviates by ~5σ from this constant energy flux value.

Comparing the light curve with the temporal evolution of the photon index yields evidence for a spectral hardening with increasing energy flux. We fit the photon index versus time with a constant, yielding χ^2/d.o.f. = 45.2/11 (probability of 4.5×10^{-6}) indicating a change of the photon index from day to day. This evidence is also found when displaying the photon index as a function of the energy flux between 2–10 keV as shown in Fig. 6. A linear fit gives a χ^2/d.o.f. of 14.0/10 (probability of 0.17). Thus, a harder-when-brighter behavior is observed during the campaign. Although spectral and flux variability in the X-ray band were previously reported in Aleksić et al. (2014a), a harder-when-brighter trend for these observations was not found.

The hydrogen column density stayed constant during the campaign (χ^2/d.o.f. = 13.4/11, probability of 0.26 for a constant fit) and is consistent with the Galactic value for IC 310 ($0.12 \times 10^{22}\,\text{cm}^{-2}$) from Kalberla et al. (2010) taking into account the large systematic uncertainties (~30%) of the survey. Hence, no conclusions can be drawn on intrinsic photo-absorption during the campaign.

For the investigation of the multi-wavelength SED, all data taken in 2012 November and December were combined to derive an averaged spectrum during the campaign. The result is shown in Fig. 7. It can be well described with a simple absorbed power-law in the range 0.5–10 keV with a hard photon spectral index of $\Gamma = 2.036^{+0.022}_{-0.019}$. This index is comparable within the errors with the index of the averaged spectrum obtained from measurements at the beginning of the year 2012.

From the INTEGRAL data, a 1σ upper limit is extracted from the variance of the stacked mosaic image at the source position taking into account a photon index of 2.0, which is extrapolated from the *Swift*-XRT band. This results in an upper limit of the energy flux of $2.9 \times 10^{-12}\,\text{erg}\,\text{cm}^{-2}\,\text{s}^{-1}$ at 110 keV in the energy range 20–200 keV. Assuming a softer photon index of 2.5, the upper limit yields $1.7 \times 10^{-12}\,\text{erg}\,\text{cm}^{-2}\,\text{s}^{-1}$ at 110 keV in the energy range 20–200 keV. For the broadband SED in Fig. 10, we show the 2σ upper limit calculated for the photon index of 2.0 and multiply it with a factor of 1.5 for the root mean square of the significance map.

The BAT data yield an energy flux of $(3.2 \pm 1.4) \times 10^{-12}\,\text{erg}\,\text{cm}^{-2}\,\text{s}^{-1}$ for the energy range 20–100 keV and a photon index of 1.8 ± 1.1 for the 104-month *Swift*-BAT survey maps with a signal-to-noise ratio of 1.85σ. Uncertainties are given at a 90% confidence level. For the broadband SED, we used the energy flux value instead of an upper limit. We applied the criterion of 3σ for the calculation of energy flux upper limits. But, as three times the 1σ energy flux uncertainty is smaller than the
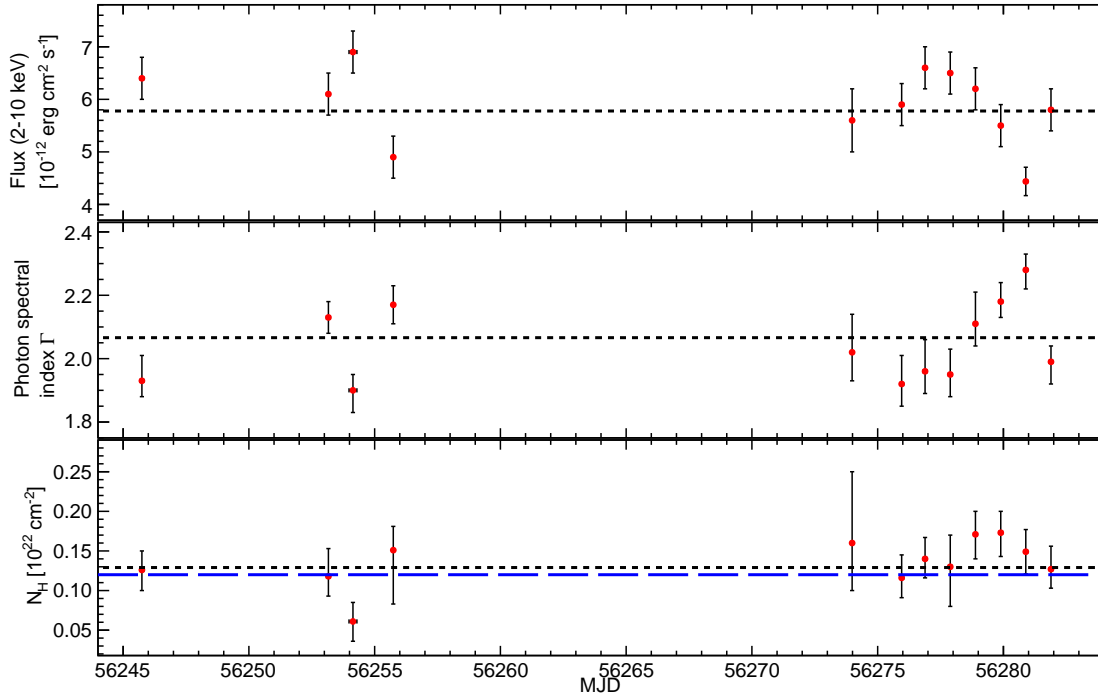
Fig. 5. *Swift*-XRT measurements during the campaign. All points have been fit with a constant (black dashed line). *Top panel:* X-ray light curve in an energy range of 2–10 keV. *Middle panel:* photon spectral index. *Bottom panel:* neutral hydrogen column density. For comparison, the Galactic N_H value of 0.12×10^{22} cm^{-2} for IC 310 (Kalberla et al. 2010) is shown as a dashed blue line.

Table 4. *Swift*-XRT X-ray spectral measurements from observations in 2012 January and 2012 November to December.

Obs. ID	MJD start	Exps. [s]	$F_{2-10\,keV} \times 10^{-11}$ [erg s^{-1} cm^{-2}]	Γ	N_H [10^{22} cm^{-2}]	χ^2/d.o.f.
2012 Jan.		13 214	0.438 ± 0.015	$2.10^{+0.05}_{-0.04}$	$0.125^{+0.015}_{-0.029}$	58.9/75
00032264001	55 952.65	2989	0.40 ± 0.04	$2.07^{+0.10}_{-0.07}$	$0.10^{+0.06}_{-0.04}$	18.9/17
00032264003	55 953.58	2885	0.37 ± 0.03	$2.18^{+0.12}_{-0.09}$	0.18 ± 0.05	11.7/15
00032264004	55 954.12	2742	$0.48^{+0.09}_{-0.07}$	$2.10^{+0.15}_{-0.09}$	0.14 ± 0.04	9.3/17
00032264005	55 955.12	3094	$0.48^{+0.04}_{-0.06}$	2.13 ± 0.06	0.12 ± 0.04	24.5/22
00032264006	55 956.14	1504	0.45 ± 0.05	$2.03^{+0.09}_{-0.10}$	$0.11^{+0.05}_{-0.06}$	14.6/8
2012 Nov.–Dec.		45 773	0.606 ± 0.010	$2.036^{+0.022}_{-0.019}$	0.135 ± 0.008	222.4/240
00032264007	56 245.67	4977	0.64 ± 0.04	$1.93^{+0.08}_{-0.05}$	$0.126^{+0.024}_{-0.026}$	37.3/38
00032264008	56 253.09	3984	0.61 ± 0.04	2.13 ± 0.05	$0.118^{+0.035}_{-0.025}$	43.8/36
00032264009	56 253.98	3968	0.69 ± 0.04	$1.90^{+0.05}_{-0.07}$	$0.061^{+0.024}_{-0.025}$	32.9/31
00032264010	56 255.70	3991	0.49 ± 0.04	2.17 ± 0.06	$0.151^{+0.030}_{-0.068}$	22.3/23
00032264011	56 273.95	1983	0.56 ± 0.06	$2.02^{+0.12}_{-0.09}$	$0.16^{+0.09}_{-0.06}$	7.3/11
00032264012	56 275.88	3891	0.59 ± 0.04	$1.92^{+0.09}_{-0.07}$	$0.116^{+0.029}_{-0.025}$	29.6/28
00032264013	56 276.81	3878	0.66 ± 0.04	$1.96^{+0.10}_{-0.07}$	$0.140^{+0.027}_{-0.024}$	34.3/31
00032264014	56 277.81	3878	0.65 ± 0.04	$1.95^{+0.08}_{-0.07}$	$0.13^{+0.04}_{-0.05}$	23.2/30
00032264015	56 278.82	3660	0.62 ± 0.04	$2.11^{+0.10}_{-0.07}$	$0.171^{+0.029}_{-0.031}$	37.7/29
00032264016	56 279.82	3864	0.55 ± 0.04	$2.18^{+0.06}_{-0.05}$	$0.173^{+0.027}_{-0.030}$	23.1/30
00032264017	56 280.82	3856	0.44 ± 0.03	$2.28^{+0.05}_{-0.06}$	0.149 ± 0.028	47.3/28
00032264018	56 281.82	3844	0.58 ± 0.04	$1.99^{+0.05}_{-0.07}$	$0.127^{+0.029}_{-0.024}$	31.9/28

Notes. Energy fluxes in the range 2–10 keV were determined by a simple absorbed power-law fit. The photon index Γ is defined following $F \propto E^{-\Gamma}$. N_H denotes the absorption with an equivalent column of hydrogen.
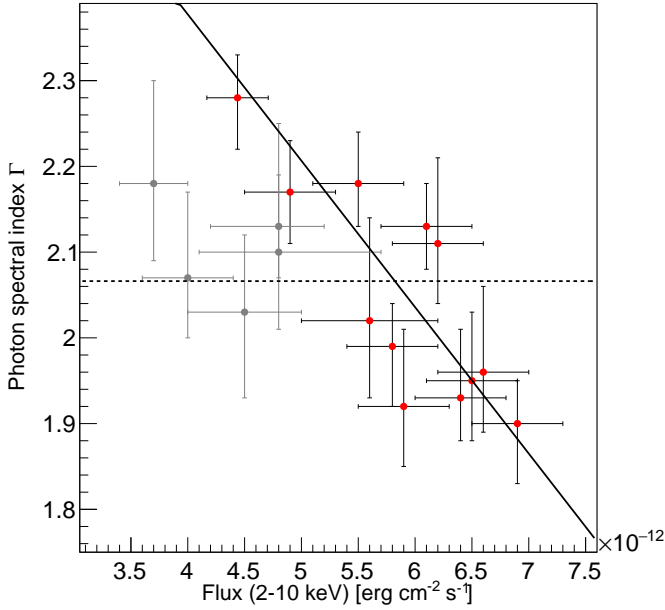
Fig. 6. Power-law index of X-ray spectra as a function of the energy flux (2–10 keV) measured by *Swift*-XRT. The dashed and solid lines represent a fit to the data with a constant and a linear function, respectively. Red points show the results from individual pointing during the MWL campaign. Additionally, gray points represent the 2012 January data.
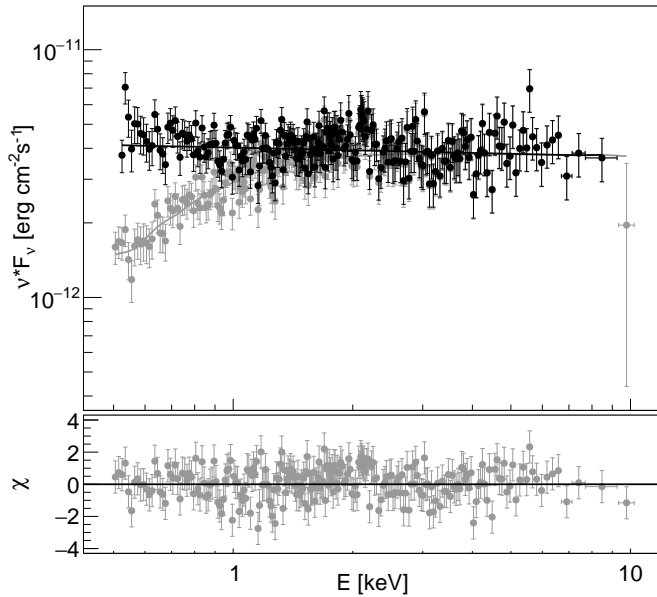

Fig. 7. Averaged spectral energy distribution from *Swift*-XRT observations from 2012 November to December. The measured spectrum is shown with gray points and is fit with an absorbed power-law function (gray lines). Fit results are given in Table 4. The de-absorbed spectrum is shown with black points and black lines. *Top panel:* resulting spectra in the energy range 0.5–10 keV. *Bottom panel:* residual of the observed spectrum.

energy flux measurement, we did not classify the energy flux as an upper limit.

3.4. Optical and UV

The KVA *R*-band optical light curve is shown in Fig. 9 and does not show any signs of variability. The light curve in the time

Table 5. *Swift*-UVOT observations.

Obs. ID 000...	MJD start	Exps. [ks]	Filter
32264001	55 952.65	2.9	*U*
32264003	55 953.58	2.8	*UVW2*
32264004	55 954.12	2.7	*UVM2*
32264005	55 955.12	3.0	*UVW1*
32264006	55 956.14	1.0	*U*
32264007	56 245.67	4.8	all
32264008	56 253.09	3.9	*UVW2*
32264009	56 253.98	3.9	*UVW2*
32264010	56 255.70	3.9	*UVW1*
32264011	56 273.95	1.9	all
32264012	56 275.88	3.8	all
32264013	56 276.81	3.7	all
32264014	56 277.81	3.7	all
32264015	56 278.82	3.5	all
32264016	56 279.82	3.7	all
32264017	56 280.82	3.7	all
32264018	56 281.82	3.7	all

Table 6. *Swift*-UVOT optical/UV flux density measurements from observations in 2012 November to December.

Filter	Freq. [Hz]	$F \times 10^{-12}$ [erg cm^{-2} s^{-1}]	$F_{\text{de-reddened}} \times 10^{-12}$ [erg cm^{-2} s^{-1}]
V	5.48×10^{14}	27.90 ± 1.18	53.96 ± 2.28
B	6.83×10^{14}	14.82 ± 0.54	35.64 ± 1.29
U	8.65×10^{14}	4.69 ± 0.25	$13.58 \pm 0.0.73$
UVW1	1.15×10^{15}	2.05 ± 0.16	8.52 ± 0.67
UVM2	1.33×10^{15}	1.09 ± 0.09	7.86 ± 0.66
UVW2	1.55×10^{15}	1.10 ± 0.08	6.35 ± 0.46

Notes. The third and fourth column report the observed and de-reddened mean values, respectively.

range of 2012 November 12 to 2013 February 02 (MJD 56 243–56 325) is consistent with a constant flux density of (9.08 ± 0.04) mJy (χ^2/d.o.f. = 5.3/17, probability of 0.99). As no further historical monitoring in the *R*-band was conducted for IC 310, the flux density cannot be compared with other measurements.

An overview of the observations from 2012 November to December by *Swift*-UVOT is given in Table 5 together with the 2012 January measurements. The results show no significant variability for any of the filters (Fig. 8). A constant fit to the 2012 November to December data revealed no variability for *B*, *U*, *V*, *UVW1* with a fit probability of 0.98, 0.99, 0.95, and 0.98, respectively. Smaller fit probabilities were obtained for the *UVM2* and *UVW2* measurements (0.26 and 0.03). Comparing the measurements in 2012 January and 2012 November-December, only at the highest frequencies (*UVM2* and *UVW2*) the mean flux densities from late 2012 are not compatible within the errors with the measurements in early 2012.

To interpret and model the broadband SED, mean flux densities for each frequency were calculated from the data taken in 2012 November to December. The values obtained are listed in Table 6. The SED in Fig. 10 shows the observed and de-reddened KVA and mean data from *Swift*-UVOT using the absorption measurement from *Swift*-XRT.
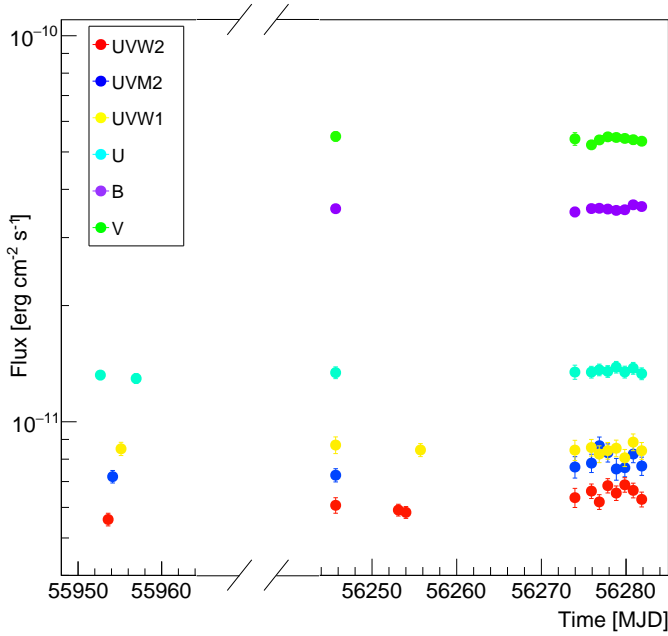
Fig. 8. Multi-frequency energy flux light curve of IC 310 obtained from *Swift*-UVOT observations. The markers for the different frequencies are indicated in the legend. All data are de-reddened using $N_{\rm H} = 0.13 \times 10^{22}\,{\rm cm^{-2}}$. To show the results from the 2012 January as well as the 2012 November to December observations simultaneously, the *x*-axis has been interrupted, as indicated by the diagonal lines. We note that the *y*-axis uses a logarithmic scale.

3.5. Radio band

The light curve at 15 GHz obtained by the OVRO monitoring program is shown in Fig. 9. From a fit of the data points from 2012 October 30 to December 23 (MJD 56 230–56 284) to a constant, a mean flux density of (0.151 ± 0.002) mJy is measured with a χ^2/d.o.f. of 31.1/13 and rather low probability of 0.003 for being constant.

From the EVN and MOJAVE data, the core and total flux density were calculated and included in Fig. 10. The estimated uncertainties for the EVN flux density measurements at 1.7, 5.0, 8.4 GHz are 10% and for 22 GHz, 15%. For the MOJAVE data we adopted an uncertainty of 5% for the total flux density (Lister & Homan 2005). We use the results from the 5.0 GHz observation taken from Aleksić et al. (2014c).

4. Discussion

In the following we discuss the results in terms of multi-frequency flux variability and interpret the broadband SED.

4.1. Multi-frequency flux variability

The combined multi-wavelength light curve is shown in Fig. 9. An exceptional TeV flare was found by MAGIC in November 2012. IC 310 remained active at VHE even after the flare. Only *Fermi*-LAT, *Swift*-BAT and partially KVA observed simultaneous to MAGIC on 2012 November 12–13. However, IC 310 could not be detected with the first two instruments during the

TeV flare and the optical emission observed by KVA is dominated by the host galaxy.

Contemporaneous measurements starting after the flare indicated a high and variable state of the object in the soft X-ray range. This marks the first time that a contemporaneous measurement of the VHE and the soft X-ray flux is reported for IC 310.

Conclusions on a correlation between the two bands should be drawn with caution because historical simultaneous measurements in both energy ranges are missing. However, considering the harder-when-brighter trend in the VHE and X-ray bands reported in Figs. 4 and 6, one can speculate that these two bands may be connected.

A harder-when-brighter behavior is frequently observed for other sources such as high-frequency peaked BL Lac (HBL) objects (Pian et al. 1998; Giommi et al. 2000; Aleksić et al. 2013, 2015; Furniss et al. 2015; Kapanadze et al. 2016; Ahnen et al. 2016a; Baloković et al. 2016). Here, the increase of the X-ray and VHE flux is combined with a hardening of the spectrum. This is consistent with the synchrotron self-Compton (SSC) mechanism, see Sect. 4.2.2. The first hump in the SED moves toward higher frequencies. The same happens for the second hump, as during a higher flux state the synchrotron photons in the low energy band are seeds for the inverse-Compton emission observed in the high-energy bands. If such a behavior is observed for a blazar with a small viewing angle, one should expect the same also for radio galaxies. This would be in line with the unified model by Urry & Padovani (1995). We note that X-ray data from other misaligned blazars (e.g., NGC 1275) often show complex emission, with a non-pure power-law and extended jet emission or X-ray emission of the filaments (Fabian et al. 2011).

The optical light curve does not show a significantly higher flux or variability. The lack of optical variability is consistent with the result of the SED modeling (see Sect. 4.2.3). The optical-infrared emission is ascribed entirely to the host galaxy, while the variable jet emission starts to dominate in the far-UV and soft X-ray band. The radio light curve indicates weak variability. As radio flares combined with an appearance of a new radio component in the VLBI images are sometimes found a few months after a gamma-ray flare Acciari et al. (2009), the time period covered here is too short to draw conclusions.

Generally, the VHE flare might be interpreted as an injection of fresh electrons and positrons into the SSC emission region. One possible origin of these particles could be the electro-magnetic cascades in the gap region of magnetospheric models resulting in an increased number of e^+e^--pairs (Beskin et al. 1992; Rieger & Mannheim 2000; Neronov & Aharonian 2007; Levinson & Rieger 2011). Such a model has been used to explain the flaring activity from M 87 by Levinson & Rieger (2011) as well as the minute timescale variability of the gamma-ray emission of IC 310 at the beginning of the MWL campaign reported by Aleksić et al. (2014c) and critically examined in Hirotani & Pu (2016). Since the magnetic field is assumed to be along the jet axis, these particles should then move along the jet and maybe also into the emission region that we observed after the flare. This could cause a higher flux in the X-ray regime as well as at VHE. We note that the quiescent state of IC 310 might be undetectable with MAGIC as sometimes IC 310 could not be detected over a long observation time (Aleksić et al. 2012). Furthermore, these fresh particles moving along the jet could also explain a general activity in the radio band.
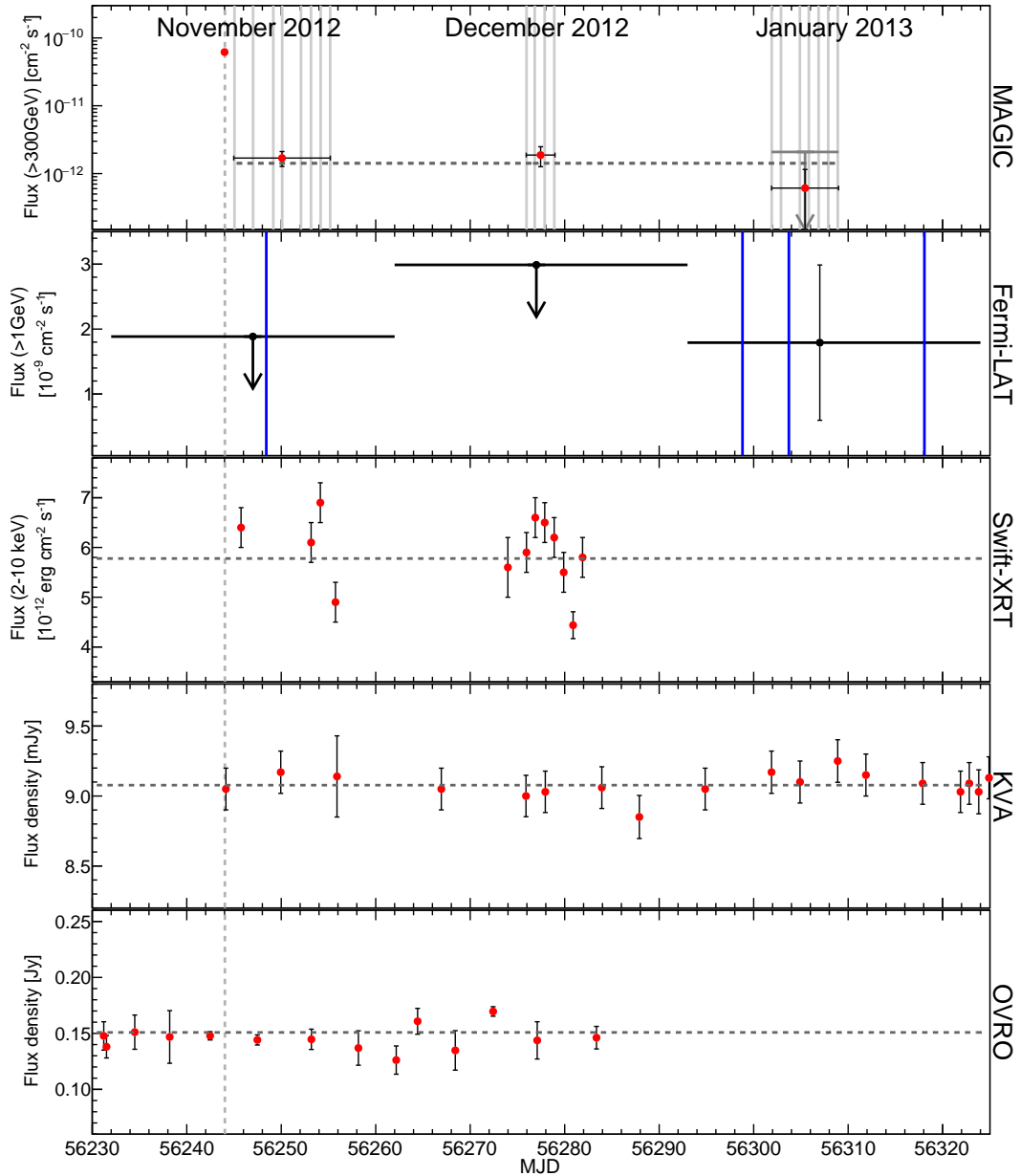
Fig. 9. Multi-wavelength light curve of IC 310 between 2012 November and 2013 January. The vertical gray dashed line indicates the day of the TeV flare. The horizontal gray dashed lines are the fits to the data with a constant. *From top to bottom:* MAGIC monthly flux measurements above 300 GeV. In addition, for 2013 January a flux 95% confidence level upper limit is calculated. The gray lines indicate the individual days when observations were performed with MAGIC. We note that the *y*-axis uses a logarithmic scale. *Fermi*-LAT above 1 GeV, blue lines indicate the arrival times of gamma-ray event candidates. *Swift*-XRT fluxes between 2–10 keV. *R*-band flux measurements by KVA (not corrected for the contribution of the host galaxy). OVRO fluxes at 15 GHz.

4.2. Modeling of the spectral energy distribution

4.2.1. Simultaneity of the data

Due to the variable behavior of IC 310 in some frequency bands (Aleksić et al. 2014a,c), SED fitting requires simultaneous data. In the VHE regime, the emission of IC 310 after the flare was rather faint, but still detectable over a long time range spanning over three months. Therefore, we calculated one spectrum over the entire observation time. For the SED, one averaged spectrum from the *Swift*-XRT observation was calculated. In the high energy range, the *Fermi*-LAT measurements are covering the time period from 2012 November 1 to 2013 January 31. The HE data is contemporaneous to the

MAGIC and *Swift*-XRT/UVOT observations. Furthermore, we included the archival spectra from the 3FGL (Acero et al. 2015) and 2FHL catalogs (Ackermann et al. 2016). The former was recorded from 2008 August−2012 July and does not cover the time of the campaign, whereas the 2FHL outlasts the campaign. The results from BAT were extracted from the long-term 104-month survey running from 2004 December to 2013 August, and are taken as an average measurement. INTEGRAL observations cover the time range from 2012 August to 2013 February and therefore are quasi-simultaneous. The optical data from KVA were coordinated with the MAGIC observations and are therefore simultaneous to those. The radio data from EVN and MO-JAVE have been included on a quasi-simultaneous basis. To
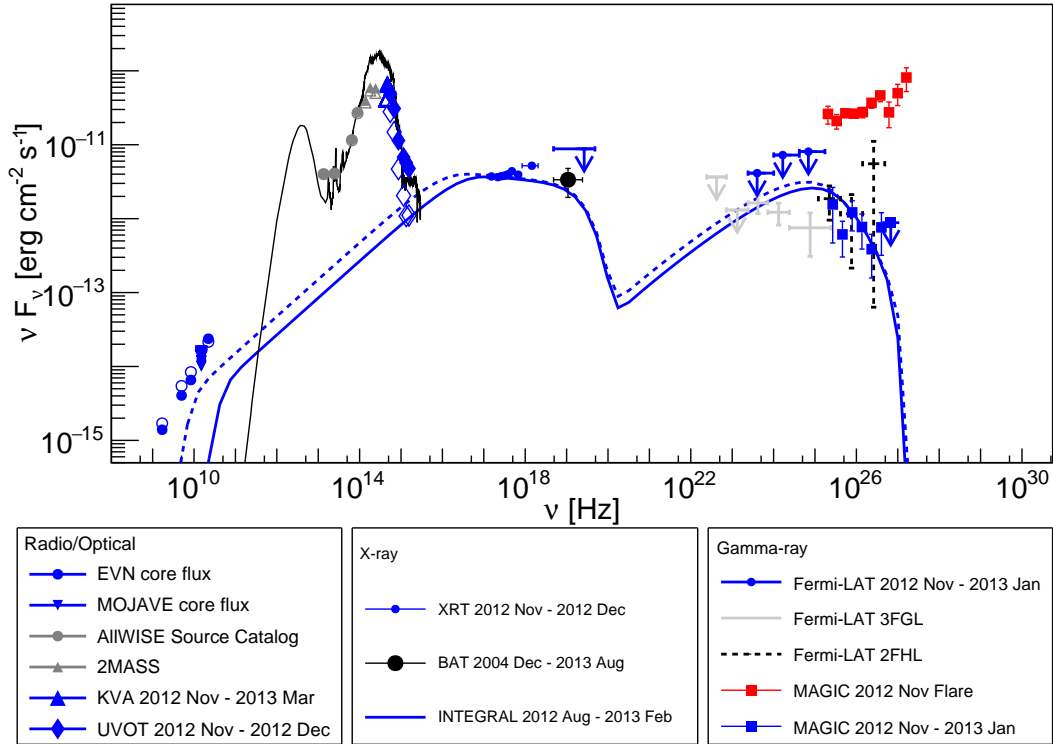
Fig. 10. Contemporaneous broadband spectral energy distribution during the MWL campaign from 2012 November to 2013 January (blue points). Individual data points are explained in the legends. Long-term averaged (if they outlast the campaign) and archival measurements are shown in black and gray, respectively. The MAGIC data points were de-absorbed using the EBL model by Domínguez et al. (2011). The red points show the derived SED of the flare observed at the beginning of the campaign, and reported in Aleksić et al. (2014c). The *Fermi*-LAT upper limits were calculated for the time period 2012 November to 2013 January. In addition, the data points from the 3FGL (Acero et al. 2015) and 2FHL catalogs (Ackermann et al. 2016) are shown. The XRT data were averaged over the entire campaign, de-absorbed with an equivalent column of hydrogen and re-binned to eight points. The data from 2MASS, AllWISE, KVA, and UVOT (open markers) have been de-reddened (filled markers) according to the XRT data. The open markers in the radio band indicate the measured total flux density, whereas the filled markers are the core flux density values. The 5.0 GHz measurement is taken from Aleksić et al. (2014c). The blue lines were obtained from a modeling of the data with a single-zone SSC model from Krawczynski et al. (2004). The solid and dashed lines are the model with a viewing angle of 10° and 20°, respectively. The black line represents a template SED for an S0 host galaxy from Polletta et al. (2007).

model the host galaxy, we also included non-simultaneous data from 2MASS and *WISE* that were recorded during 1997 June to 2001 February and 2010 January to 2010 November, respectively.

4.2.2. Model description

The SED of a jet-dominated radio-loud AGN can be explained by non-thermal emission of accelerated particles. In the shock-in-jet model (Blandford & Königl 1979), these particles are accelerated at shock waves in the jet which can originate, for example, from density fluctuations of the plasma. The low-energy emission of the double-humped SED of radio-loud AGNs is explained by synchrotron radiation of the electrons and positrons due to the magnetic fields in the jets. In contrast, the origin of the higher energy hump is still a matter of debate. Leptonic (inverse) Compton scattering (Marscher & Gear 1985; Maraschi et al. 1992; Bloom & Marscher 1996), and hadronic – for example, proton synchrotron (Mannheim 1993b; Mücke et al. 2003) and neutral pion decay initiated electromagnetic cascades (Mannheim 1993a) – processes can lead to the emission observed at higher frequencies. As shown in Aleksić et al. (2014c), this shock-in-jet model cannot explain the fast TeV flare in 2012 November.

As mentioned in Sect. 4.1, freshly injected electrons and positrons may result from electro-magnetic cascades inside a gap region of a pulsar-like magnetosphere surrounding the central black hole. The acceleration of the particles due to the huge electric potential in the gap and emission via inverse-Compton and curvature radiation can explain the flaring behavior as reported in Aleksić et al. (2014c). However, after some time, the gap short-circuited because the charge density reaches the Goldreich-Julian charge density and the cascading stops. The particles may move in the direction of the jet.

We adopt the single-zone SSC model by (Krawczynsk et al. 2004) to model the broadband SED. The model consists of the following parameters: the bulk Lorentz factor Γ_b, the viewing angle θ, the magnetic field B, the radius of the emission region R, the electron energy density U_e, the ratio η of the electron energy density to the magnetic field energy density U_B, the minimal energy and the maximal energy of the electrons E_{min} and E_{max}, the break energy E_{break}, and the spectral indices p_i ($dN/dE \propto E^{-p_i}$, E is the electron energy in the jet frame). In this model it is assumed that the electrons follow a broken power-law energy spectrum with the indices p_1 for the energies E_{min} to E_{break} and p_2 for E_{break} to E_{max}.

We assume a viewing angle of $10° \lesssim \theta \lesssim 20°$ as found by Aleksić et al. (2014c). For this range of viewing angles, a rather low bulk Lorentz factor is necessary to enable having at least a

Table 7. Model parameters for the one-zone SSC model describing the broadband SED of IC 310.

Γ	δ	θ [°]	p_1	p_2	$E_{\min}$ log10(E/eV)	$E_{\max}$ log10(E/eV)	E_{break} log10(E/eV)	U_{e} [erg/cm^3]	η [U_{e}/U_B]	B [G]	R [cm]
5	5.7	10	2.0	3.1	5.7	12.0	10.6	0.21	59	0.3	2.1×10^{15}
5	2.5	20	2.0	3.1	5.7	12.4	10.8	0.012	30	0.1	3.0×10^{16}

Notes. Resulting model curves are depicted in Fig. 10.

moderate Doppler boosting. Here, we use $\Gamma_b = 5$. We note that the models applied to the data are only two possibilities, one for $\theta = 10°$ and one for $\theta = 20°$; generally, a large degeneracy of parameters exists (Ahnen et al. 2016b). In addition to the SSC model, a template SED for a galaxy of morphology type S0 (Polletta et al. 2007) is added to account for the strong dominance of the host galaxy in the infrared to UV range as observed from the S0-type galaxy IC 310 (de Vaucouleurs et al. 1991)[11].

4.2.3. Results

The broadband SED is shown in Fig. 10. Apart from the radio telescopes, the angular resolution of all other instruments used in this paper is a limitation to study a jetted object such as IC 310. Detailed radio observations do not indicate, for example, lobe emission (Sijbring & de Bruyn 1998; Kadler et al. 2012). Moreover, deep X-ray measurements show a mostly point-like emission positionally consistent with the bright radio core (Dunn et al. 2010). Therefore, when modeling the broadband SED, we consider that all emission is coming from around the central region of the AGN.

The core fluxes from the radio VLBI data follow a typical flat spectrum with a constant flux density. The hard spectrum in the soft X-ray regime suggests that the synchrotron emission peaks in the νF_ν representation in the soft X-ray band and declines in the hard X-ray band as indicated by the *Swift*-BAT and INTEGRAL data, though both are not strictly simultaneous to the *Swift*-XRT measurements. The *Fermi*-LAT upper limits are consistent with the long-term spectrum from the 3FGL catalog. The MAGIC spectrum of the campaign yields a similar flux state as the 2FHL catalog data and also follows the high energy points of the 3FGL spectrum. These three spectra, even though they only have a partial temporal overlap, show that the high energy spectral index is very hard in the GeV range ($\Gamma_{\text{3FGL}} = 1.90 \pm 0.14$, $\Gamma_{\text{2FHL}} = 1.34 \pm 0.42$) and that the second hump is located below 100 GeV during the campaign. However, during the TeV flare, the peak frequency of the second hump is above 10 TeV and therefore, shifted by more than two orders of magnitude. The hard VHE spectrum extending to 10 TeV cannot be reproduced within a one-zone SSC scenario because of the strong Klein-Nishina suppression at multi TeV energies. Instead, Hirotani & Pu (2016) were able to reproduce the flux and the hard spectrum during the flare of IC 310 with a superposition of curvature emission in the magnetosphere with varying curvature radii. Spectral variability in the TeV band can be explained by, for example, different accretion rates in this model.

In general, the SED reveals that the object has been measured in a state of rather low TeV activity after the VHE flare on 2012 November 12–13 and in a high state in the X-ray band.

This is the first time that both regimes have been measured simultaneously, so one cannot make a statement concerning the occurrence of a simultaneous low and high state in both bands.

The measured SED of IC 310 seems to follow a simple, featureless double-hump structure besides the host galaxy emission, as seen from blazars. A single-zone SSC model is able to explain the broadband emission in general, though it is not possible to reproduce the flux densities of the VLBI core measurements which likely comprise additional radio emission from other regions. The radio and X-ray data suggest a broad synchrotron emission hump which can be explained with a large maximal Lorentz factor of the particles. This agrees with the second hump peaking in the GeV range or even higher. However, it is difficult to fit the 3FGL, 2FHL, and low-state MAGIC data simultaneously with an SSC model due to the broadness of the second hump. The SSC model curves are, however, consistent with the upper limits in the GeV band calculated for this campaign.

The parameters of the SSC models used for the magnetic field, the radius of the emission region, and the necessary Lorentz factors of the particles are in agreement with the constraints from the magnetospheric model used to explain the emission from the TeV flare (Aleksić et al. 2014c). Here, we assume that the emission region is caused by a cloud formed out of the particles created due to the cascading in the gap region during the flaring period. This blob moves away from the center of the AGN in the direction of a conical jet with a distance d corresponding to a travel time of 1–2 months. Here, the magnetic field strength reduces from the values inferred from Levinson & Rieger (2011) to the values used in the SSC models from this work, assuming the dependence of $B(d) \sim d^{-1}$ (Konigl 1981; Lobanov 1998). Furthermore, assuming a conical geometry, the radius of the emission region increases to $R \sim 10^{15}$ cm, consistent with the values used for the 10° model[12]. The required energetics of maximal $E_{\max} = 12$ (in units of log10(E/eV)) with a Lorentz factor of the particles of $\sim 10^6$ can be achieved, as even higher values were found by Hirotani & Pu (2016). The SSC code of Krawczynski et al. (2004) includes the effect of $\gamma\gamma$-pair production and for both models the optical thickness for $\gamma\gamma$-pair production is low enough for TeV emission to escape.

In the IR-optical-UV range of the SED, the emission is strongly dominated by the host galaxy. The template SED of the S0-type galaxy represents the measured data points very well. An SED for an elliptical galaxy would have overestimated the contribution in the optical range by one order of magnitude. Instead, the template we used suggests a rather strong emission in the IR band due to starburst processes. Unfortunately, NGC 1275 is too bright in the far-infrared and microwave regime, so that the emission from IC 310 could be outshone by NGC 1275 in maps obtained by the *Planck* satellite[13].

---

[11] The template from the *Spitzer* Wide-area InfraRed Extragalactic survey (SWIRE) library can be found under the following link: http://www.iasf-milano.inaf.it/~polletta/templates/swire_templates.html

[12] We assumed a radius at the starting point consistent with the variability timescale observed in Aleksić et al. (2014c).

[13] However, the angular resolution of *Planck* at high frequencies should be good enough to separate the emission from both AGNs.

Finally, we use the broadband SED to determine the mass of the central black hole analogous to Krauß et al. (2016) using the fundamental plane of black hole activity. We assume the X-ray flux of the 2012 November and December data (Table 4), the 5 GHz core flux measurement from EVN and extrapolated the EVN core data with a simple power-law spectrum in order to estimate the 1.4 GHz flux. The extrapolation was done by fitting the spectrum of the 1.7, 5.0, 8.4, and 22.2 GHz core data with a power-law of the form $dN/dE = (E/E_0)^{-\Gamma_R}$ with E_0 being a normalization flux and Γ_R the power-law index. The fitting yields $\Gamma_R = 0.95$ and thus a differential flux at 1.4 GHz of 1.08×10^{-15} erg cm^{-2} s^{-1}. The resulting masses are given in $\log_{10}(M_\odot)$: (7.89 ± 0.09) for the fundamental plane found in Gültekin et al. (2009), (8.4 ± 1.3) for Merloni et al. (2003), (9 ± 4) for Körding et al. (2006), for (8.4 ± 2.9) Bonchi et al. (2013), and (8.2 ± 1.0) for Nisbet & Best (2016)[14]. These values are consistent with $M_{BH} \simeq \left(3^{+4}_{-2}\right) \times 10^8 \, M_\odot$ reported in Aleksić et al. (2014c). Instead, Berton et al. (2015) estimated a mass for IC 310 of one order of magnitude lower than the value estimated in Aleksić et al. (2014c) based on a smaller velocity dispersion used for the $M_{BH} - \sigma$ relation. Assuming a smaller mass would somewhat weaken the arguments given in Aleksić et al. (2014c) as the variability timescale then roughly equals the event horizon light crossing time. But the opacity problem as explained in Aleksić et al. (2014c) still remains.

4.2.4. Comparsion with misaligned blazars and blazars

The SSC model parameter values reported in this study for IC 310 are similar to those obtained for misaligned blazars, for example, PKS 0625−354, 3C 78 in Fukazawa et al. (2015), Cen A core in Abdo et al. (2010a), M 87 in Abdo et al. (2009b), NGC 1275 in Abdo et al. (2009a) and Aleksić et al. (2014b), and NGC 6251 in Migliori et al. (2011)[15]. Compared to BL Lac objects, the values for the bulk Lorentz and Doppler factor are lower for IC 310 as well as the other misaligned blazars. This is understandable because the Doppler boosting is weaker as a result of the larger viewing angle. However, to maintain some boosting at larger viewing angles, a smaller bulk Lorentz factor is mandatory. Lower bulk Lorentz factors were also found for gamma-ray blazars in a quiescent state (Ahnen et al. 2016b), but large Lorentz factors are needed to explain the fast variability observed from blazars (Begelman et al. 2008). The radii for the emission region used for IC 310 coincide with the observed variability of the object in the X-ray range after the TeV flare and are comparable to those used for other misaligned blazars. Interestingly, the models for IC 310 show a higher $\gamma_{break} = 10^{E_{break}}/m_e c^2$ similar to the SEDs from PKS 0625−354, 3C 78, and NGC 6251, see Fukazawa et al. (2015) and Migliori et al. (2011). Such high γ_{break} leads to higher synchrotron peak frequencies ($\sim 10^{17}$ Hz). This is in agreement with the hard spectrum in the soft X-ray and gamma-ray band observed from IC 310. Among the misaligned blazars, IC 310 shows one of the hardest gamma-ray spectra, $\Gamma_{3FGL} = 1.90 \pm 0.14$ in the 3FGL (Acero et al. 2015), the hardest in the 2FHL catalog (Ackermann et al. 2016) with $\Gamma_{2FHL} = 1.34 \pm 0.42$, and $\Gamma_{MAGIC} = 1.8$–2.4 as reported by MAGIC here and in Aleksić et al. (2010, 2014a,c).

---

[14] The values based on Eq. (4) and the parameters from Eq. (6) by Gültekin et al. (2009) seem to under-predict the uncertainties of the black hole mass estimate.

[15] We note that the broadband SED of Cen A cannot be described by a simple one-zone SSC model due to the unusual gamma-ray spectrum (Abdo et al. 2010a).

5. Summary and conclusions

In this paper we have presented the results from the first multi-wavelength campaign from radio to the VHE range, conducted in 2012 November and 2013 January for the misaligned blazar IC 310. During the campaign, an exceptionally bright VHE flare was detected showing fast flux variability in one night. There is no significant data from the lower energy bands available for that night due to low statistics of all-sky monitors such as *Fermi*-LAT and *Swift*-BAT. After the flare, the TeV flux declined rapidly. Through early 2013, only a low but still detectable VHE emission was observed. Compared to previous measurements and combining those with the results reported in this paper, a harder-when-brighter behavior can be inferred. The same behavior is found for the soft X-ray emission during the campaign. The photon spectral index hardens with increasing flux for IC 310, which we report here for the first time. The harder-when-brighter behavior of the X-ray and VHE emission after the TeV flare is consistent with the expectations from a one-zone SSC mechanism.

Other than the variability found in the X-ray band, the multi-wavelength light curve reveals no strong variability after the TeV flare. In the GeV band, no detection with a high significance could be inferred from the *Fermi*-LAT observations. The same applies to the *Swift*-BAT observation in the hard X-ray band. The host galaxy dominates completely the optical emission, and hence the optical variability of this object could not be properly evaluated. For the investigation of the variability in the radio band, a larger period and dedicated VLBI monitoring at one frequency is necessary to make further conclusions on the changes of the pc-scale jet after the flare. This will be discussed in a forthcoming paper by Schulz et al. (in prep.).

As previously reported, the TeV flare cannot be explained with standard shock-in-jet models. An alternative suggestion is based on magnetospheric models for AGNs. According to these, charge-depleted regions in AGN-magnetospheres are the birthplaces of the highest energetic particles and electromagnetic cascades. In these cascades, a large number of electrons and positrons are produced which can in principle load the jet, letting a new blob of particles travel along the jet axis. In this paper, we discussed the possibility that this blob can be the emission zone as required in a single-zone SSC model. We have shown that this simple model can explain the broadband SED of IC 310 observed during the campaign. Furthermore, the parameters used for the SSC modeling agree with those obtained for other gamma-ray loud misaligned blazars.

References

Abdo, A. A., Ackermann, M., Ajello, M., et al. 2009a, ApJ, 699, 31
Abdo, A. A., Ackermann, M., Ajello, M., et al. 2009b, ApJ, 707, 55
Abdo, A. A., Ackermann, M., Ajello, M., et al. 2010, ApJ, 719, 1433
Acciari, V. A., Beilicke, M., Blaylock, G., et al. 2008, ApJ, 679, 397
Acciari, V. A., Aliu, E., Arlen, T., et al. 2009, Science, 325, 444
Acero, F., Ackermann, M., Ajello, M., et al. 2015, ApJS, 218, 23
Acero, F., Ackermann, M., Ajello, M., et al. 2016, ApJS, 223, 26
Ackermann, M., Ajello, M., Albert, A., et al. 2012, ApJS, 203, 4
Ackermann, M., Ajello, M., Atwood, W. B., et al. 2016, ApJS, 222, 5
Aharonian, F., Akhperjanian, A., Beilicke, M., et al. 2003, A&A, 403, L1
Aharonian, F., Akhperjanian, A. G., Bazer-Bachi, A. R., et al. 2006, Science, 314, 1424
Aharonian, F., Akhperjanian, A. G., Anton, G., et al. 2009, ApJ, 695, L40
Ahnen, M. L., Ansoldi, S., Antonelli, L. A., et al. 2016a, MNRAS, 459, 2286
Ahnen, M. L., Ansoldi, S., Antonelli, L. A., et al. 2016b, A&A, accepted [arXiv:1612.09472]
Albert, J., Aliu, E., Anderhub, H., et al. 2008, ApJ, 685, L23
Aleksić, J., Antonelli, L. A., Antoranz, P., et al. 2010, ApJ, 723, L207
Aleksić, J., Alvarez, E. A., Antonelli, L. A., et al. 2012, A&A, 539, L2
Aleksić, J., Antonelli, L. A., Antoranz, P., et al. 2013, A&A, 556, A67
Aleksić, J., Antonelli, L. A., Antoranz, P., et al. 2014a, A&A, 563, A91
Aleksić, J., Ansoldi, S., Antonelli, L. A., et al. 2014b, A&A, 564, A5
Aleksić, J., Ansoldi, S., Antonelli, L. A., et al. 2014c, Science, 346, 1080
Aleksić, J., Ansoldi, S., Antonelli, L. A., et al. 2015, A&A, 576, A126
Aleksić, J., Ansoldi, S., Antonelli, L. A., et al. 2016a, Astropart. Phys., 72, 61
Aleksić, J., Ansoldi, S., Antonelli, L. A., et al. 2016b, Astropart. Phys., 72, 76
Atwood, W. B., Abdo, A. A., Ackermann, M., et al. 2009, ApJ, 697, 1071
Baloković, M., Paneque, D., Madejski, G., et al. 2016, ApJ, 819, 156
Begelman, M. C., Fabian, A. C., & Rees, M. J. 2008, MNRAS, 384, L19
Bernardi, M., Alonso, M. V., da Costa, L. N., et al. 2002, AJ, 123, 2990
Berton, M., Foschini, L., Ciroi, S., et al. 2015, A&A, 578, A28
Beskin, V. S., Istomin, Y. N., & Parev, V. I. 1992, Sov. Astron., 36, 642
Blandford, R. D., & Königl, A. 1979, ApJ, 232, 34
Bloom, S. D., & Marscher, A. P. 1996, ApJ, 461, 657
Bonchi, A., La Franca, F., Melini, G., Bongiorno, A., & Fiore, F. 2013, MNRAS, 429, 1970
Burrows, D. N., Hill, J. E., Nousek, J. A., et al. 2005, Space Sci. Rev., 120, 165

de Vaucouleurs, G., de Vaucouleurs, A., Corwin, Jr., H. G., et al. 1991, Third Reference Catalogue of Bright Galaxies. Volume I: Explanations and references. Volume II: Data for galaxies between 0 h and 12 h. Volume III: Data for galaxies between 12 h and 24 h
Domínguez, A., Primack, J. R., Rosario, D. J., et al. 2011, MNRAS, 410, 2556
Dunn, R. J. H., Allen, S. W., Taylor, G. B., et al. 2010, MNRAS, 404, 180
Dyrda, M., Wierzcholska, A., Hervet, O., et al. 2015, ArXiv e-prints [arXiv:1509.06851]
Fabian, A. C., Sanders, J. S., Williams, R. J. R., et al. 2011, MNRAS, 417, 172
Fukazawa, Y., Finke, J., Stawarz, Ł., et al. 2015, ApJ, 798, 74
Furniss, A., Noda, K., Boggs, S., et al. 2015, ApJ, 812, 65
Gehrels, N., Chincarini, G., Giommi, P., et al. 2004, ApJ, 611, 1005
Giommi, P., Padovani, P., & Perlman, E. 2000, MNRAS, 317, 743
Gültekin, K., Cackett, E. M., Miller, J. M., et al. 2009, ApJ, 706, 404
Hirotani, K., & Pu, H.-Y. 2016, ApJ, 818, 50
Houck, J. C., & Denicola, L. A. 2000, in Astronomical Data Analysis Software and Systems IX, eds. N. Manset, C. Veillet, & D. Crabtree, ASP Conf. Ser., 216, 591
Kadler, M., Eisenacher, D., Ros, E., et al. 2012, A&A, 538, L1
Kalberla, P. M. W., McClure-Griffiths, N. M., Pisano, D. J., et al. 2010, A&A, 521, A17
Kapanadze, B., Romano, P., Vercellone, S., et al. 2016, MNRAS, 457, 704
Konigl, A. 1981, ApJ, 243, 700
Körding, E., Falcke, H., & Corbel, S. 2006, A&A, 456, 439
Krauß, F., Wilms, J., Kadler, M., et al. 2016, A&A, 591, A130
Krawczynski, H., Hughes, S. B., Horan, D., et al. 2004, ApJ, 601, 151
Levinson, A., & Rieger, F. 2011, ApJ, 730, 123
Li, T.-P., & Ma, Y.-Q. 1983, ApJ, 272, 317
Lister, M. L., & Homan, D. C. 2005, AJ, 130, 1389
Lister, M. L., Aller, H. D., Aller, M. F., et al. 2009, AJ, 137, 3718
Lister, M. L., Aller, M. F., Aller, H. D., et al. 2016, AJ, 152, 12
Lobanov, A. P. 1998, A&A, 330, 79
Mannheim, K. 1993a, Phys. Rev. D, 48, 2408
Mannheim, K. 1993b, A&A, 269, 67
Maraschi, L., Ghisellini, G., & Celotti, A. 1992, ApJ, 397, L5
Marscher, A. P., & Gear, W. K. 1985, ApJ, 298, 114
Mattox, J. R., Bertsch, D. L., Chiang, J., et al. 1996, ApJ, 461, 396
Merloni, A., Heinz, S., & di Matteo, T. 2003, MNRAS, 345, 1057
Migliori, G., Grandi, P., Torresi, E., et al. 2011, A&A, 533, A72
Miley, G. 1980, ARA&A, 18, 165
Mücke, A., Protheroe, R. J., Engel, R., Rachen, J. P., & Stanev, T. 2003, Astropart. Phys., 18, 593
Neronov, A., & Aharonian, F. A. 2007, ApJ, 671, 85
Neronov, A., Semikoz, D., & Vovk, I. 2010, A&A, 519, L6
Nisbet, D. M., & Best, P. N. 2016, MNRAS, 455, 2551
Owen, F. N., Ledlow, M. J., & Keel, W. C. 1996, AJ, 111, 53
Pian, E., Vacanti, G., Tagliaferri, G., et al. 1998, ApJ, 492, L17
Polletta, M., Tajer, M., Maraschi, L., et al. 2007, ApJ, 663, 81
Rector, T. A., Stocke, J. T., & Perlman, E. S. 1999, ApJ, 516, 145
Rhee, G., Burns, J. O., & Kowalski, M. P. 1994, AJ, 108, 1137
Richards, J. L., Max-Moerbeck, W., Pavlidou, V., et al. 2011, ApJS, 194, 29
Rieger, F. M., & Mannheim, K. 2000, A&A, 353, 473
Rolke, W. A., López, A. M., & Conrad, J. 2005, Nucl. Instr. Methods A, 551, 493
Ryle, M., & Windram, M. D. 1968, MNRAS, 138, 1
Sato, K., Furusho, T., Yamasaki, N. Y., et al. 2005, PASJ, 57, 743
Schwarz, R. A., Edge, A. C., Voges, W., et al. 1992, A&A, 256, L11
Sijbring, D., & de Bruyn, A. G. 1998, A&A, 331, 901
Sitarek, J., Carmona, E., Colin, P., et al. 2013, ArXiv e-prints [arXiv:1308.0141]
Skrutskie, M. F., Cutri, R. M., Stiening, R., et al. 2006, AJ, 131, 1163
Ubertini, P., Lebrun, F., Di Cocco, G., et al. 2003, A&A, 411, L131
Urry, C. M., & Padovani, P. 1995, PASP, 107, 803
Vedrenne, G., Roques, J.-P., Schönfelder, V., et al. 2003, A&A, 411, L63
Verner, D. A., Ferland, G. J., Korista, K. T., & Yakovlev, D. G. 1996, ApJ, 465, 487
Wilms, J., Allen, A., & McCray, R. 2000, ApJ, 542, 914
Winkler, C., Courvoisier, T. J.-L., Di Cocco, G., et al. 2003, A&A, 411, L1
Wright, E. L., Eisenhardt, P. R. M., Mainzer, A. K., et al. 2010, AJ, 140, 1868

[1] ETH Zurich, 8093 Zurich, Switzerland
[2] Università di Udine, and INFN Trieste, 33100 Udine, Italy
[3] INAF National Institute for Astrophysics, 00136 Rome, Italy
[4] Università di Padova and INFN, 35131 Padova, Italy
[5] Croatian MAGIC Consortium, Rudjer Boskovic Institute, University of Rijeka, University of Split – FESB, University of Zagreb – FER, University of Osijek, Croatia
[6] Saha Institute of Nuclear Physics, 1/AF Bidhannagar, Salt Lake, Sector-1, 700064 Kolkata, India
[7] Max-Planck-Institut für Physik, 80805 München, Germany
[8] Universidad Complutense, 28040 Madrid, Spain
[9] Inst. de Astrofísica de Canarias, 38200 La Laguna, Tenerife, Spain
[10] Universidad de La Laguna, Dpto. Astrofísica, 38206 La Laguna, Tenerife, Spain
[11] University of Łódź, 90236 Lodz, Poland
[12] Deutsches Elektronen-Synchrotron (DESY), 15738 Zeuthen, Germany
[13] Institut de Fisica d'Altes Energies (IFAE), The Barcelona Institute of Science and Technology, Campus UAB, 08193 Bellaterra (Barcelona), Spain
[14] Università di Siena, and INFN Pisa, 53100 Siena, Italy
[15] Universität Würzburg, 97074 Würzburg, Germany
[16] Institute for Space Sciences (CSIC/IEEC), 08193 Barcelona, Spain
[17] Technische Universität Dortmund, 44221 Dortmund, Germany
[18] Finnish MAGIC Consortium, Tuorla Observatory, University of Turku and Astronomy Division, University of Oulu, 90014 Oulu, Finland
[19] Unitat de Física de les Radiacions, Departament de Física, and CERES-IEEC, Universitat Autònoma de Barcelona, 08193 Bellaterra, Spain
[20] Universitat de Barcelona, ICC, IEEC-UB, 08028 Barcelona, Spain
[21] Japanese MAGIC Consortium, ICRR, The University of Tokyo, Department of Physics and Hakubi Center, Kyoto University, Tokai University, The University of Tokushima, Japan
[22] Inst. for Nucl. Research and Nucl. Energy, 1784 Sofia, Bulgaria
[23] Università di Pisa, and INFN Pisa, 56126 Pisa, Italy
[24] ICREA and Institute for Space Sciences (CSIC/IEEC), 08193 Barcelona, Spain
[25] Also at the Department of Physics of Kyoto University, 606-8501 Kyoto, Japan
[26] Now at Centro Brasileiro de Pesquisas Físicas (CBPF/MCTI), R. Dr. Xavier Sigaud, 150 – Urca, 22290-180 Rio de Janeiro – RJ, Brazil
[27] Now at NASA Goddard Space Flight Center, Greenbelt, MD 20771, USA and Department of Physics and Department of Astronomy, University of Maryland, College Park, MD 20742, USA
[28] Humboldt University of Berlin, Institut für Physik Newtonstr. 15, 12489 Berlin, Germany
[29] Also at University of Trieste, 34127 Trieste, Italy
[30] Now at École polytechnique fédérale de Lausanne (EPFL), 1085 Lausanne, Switzerland
[31] Now at Finnish Centre for Astronomy with ESO (FINCA), 21500 Turku, Finland
[32] Also at INAF-Trieste and Dept. of Physics & Astronomy, University of Bologna, 40126 Bologna, Italy
[33] GRAPPA & Anton Pannekoek Institute for Astronomy, University of Amsterdam, Science Park 904, 1098 XH Amsterdam, The Netherlands
[34] ASTRON, the Netherlands Institute for Radio Astronomy, PO Box 2, 7990 AA Dwingeloo, The Netherlands
[35] Dr. Remeis Sternwarte & ECAP, Universität Erlangen-Nürnberg, Sternwartstrasse 7, 96049 Bamberg, Germany
[36] Max-Planck-Institut für Radioastronomie, Auf dem Hügel 69, 53121 Bonn, Germany
[37] Departament d'Astronomia i Astrofísica, Universitat de València, C/Dr. Moliner 50, 46100 Burjassot, València, Spain
[38] Observatori Astronòmic, Universitat de València, C/Catedrático José Beltrán 2, 46980 Paterna, València, Spain
[39] NASA, Goddard Space Flight Center, Greenbelt, MD 20771, USA
[40] Department of Astrophysics/IMAPP, Radboud University Nijmegen, PO Box 9010, 6500 GL Nijmegen, The Netherlands
[41] ESA/ESTEC, Keplerlaan 1, 2201 AZ Noordwijk, The Netherlands
[42] Aalto University Metsähovi Radio Observatory, Metsähovintie 114, 02540 Kylmälä, Finland
[43] Aalto University Department of Radio Science and Engineering, PO Box 13000, 00076 Aalto, Finland
[44] Department of Physics and Department of Astronomy, University of Maryland, College Park, MD 20742, USA
[45] Landessternwarte, Universität Heidelberg, Königstuhl, 69117 Heidelberg, Germany